Frequency-Domain Reverse-Time Migration of Ground Penetrating Radar Based on Layered Medium Green's Functions

Hai Liu, *Member, IEEE*, Zhijun Long, Feng Han, *Member, IEEE*, Guangyou Fang, and Qing Huo Liu, *Fellow, IEEE*

***Abstract*—A frequency-domain reverse-time migration (RTM) algorithm based on the layered medium dyadic Green's function (DGF) is proposed for high-resolution and efficient subsurface imaging using ground penetrating radar (GPR). Different from the conventional RTM, which is performed by the finite-difference time domain (FDTD) method, both the forward and backward extrapolation wavefields in this frequency-domain RTM are computed by the multiplication between the frequency spectra of the excitation source or the recorded GPR data and the layered medium DGFs. The final image is reconstructed by the direct summation of all the wavefields for all the sampling frequencies in the frequency domain, instead of transforming them back to the time domain and processing them. Two-dimensional (2-D) or 3-D numerical and laboratory experiments show that the proposed frequency-domain RTM algorithm can yield almost the same imaging results as the conventional time domain RTM algorithm but requires less than two orders of magnitude in computational costs. The proposed GPR imaging method is verified to be competent for the fast 3-D imaging of potential larva rocks under the lunar surface, which can provide critical information for the regolith-drilling task of the Chang-E 5 lunar exploration mission of China. Real-time subsurface imaging by RTM could be fulfilled and be widely applied to engineering geophysics, such as urban utility detection, through-wall imaging, and ice monitoring by ground-coupled or air-borne GPR.**

***Index Terms*—Ground penetrating radar (GPR), layered medium Green's function, lunar exploration, reverse-time migration (RTM).**

Manuscript received December 26, 2017; revised April 9, 2018; accepted May 23, 2018. Date of publication June 13, 2018; date of current version August 21, 2018. This work was supported in part by the National Key Research and Development Program of China under Grant 2016YFC0802400 and in part by the National Natural Science Foundation of China under Grant 41504111 Grant 41504120. *(Corresponding author: Feng Han.)*

H. Liu was with the Institute of Electromagnetics and Acoustics, Department of Electronic Science, Xiamen University, Xiamen 361005, China. He is now with the School of Civil Engineering, Guangzhou University, Guangzhou 510006, China (e-mail: hliu@gzhu.edu.cn).

Z. Long and F. Han are with the Institute of Electromagnetics and Acoustics, and Department of Electronic Science, Xiamen University, Xiamen 361008, China (e-mail: long_lbj@126.com; feng.han@xmu.edu.cn).

G. Fang is with the Key Laboratory of Electromagnetic Radiation and Sensing Technology, Chinese Academy of Sciences, Beijing 100190, China (e-mail: gyfang@mail.ie.ac.cn).

Q. H. Liu is with the Department of Electrical and Computer Engineering, Duke University, Durham, NC 27708 USA (e-mail: qhliu@duke.edu).

Color versions of one or more of the figures in this paper are available online at http://ieeexplore.ieee.org.

Digital Object Identifier 10.1109/JSTARS.2018.2841361

I. Introduction

GROUND penetrating radar (GPR), as a high-efficiency near-surface geophysical tool, has been widely applied in geological mapping [1], [2], hydrological monitoring [3]–[6], nondestructive testing of civil engineering structures [7], [8], planet exploration [9]–[11], landmine detection [12], [13], etc. A portable GPR system is desired for field data acquisition, and it employees a small antenna, which exhibits low directivity and a wide beamwidth. This causes the GPR image to bear little resemblance to the actual target scattering scenario [14]. Migration can collapse the diffraction hyperbola on its apex and move the inclined reflector to its true position, and thus is often used to reconstruct the subsurface image. Various migration algorithms have been used for the GPR imaging, such as diffraction stacking [14], [15], phase-shift migration [16], [17], synthetic aperture radar processing [18], back propagation [19], [20], etc. Reviews of these migration algorithms can be found in [21] and [22].

Reverse-time migration (RTM) is based on the two-way wave equation and can be viewed as the matched filtering between the incident field and the time-reversed receiver field [23]. It has been recognized as one of the most accurate imaging methods currently available [24], [25]. Due to its high accuracy in reconstructing images of subsurface complex structures, RTM has become a routine imaging technique for the seismic exploration [26]–[28], and also has been applied to optical imaging [29], as well as GPR imaging [30]–[34] in recent years. The finite-difference time domain (FDTD) method is conventionally used to calculate the wavefields during the forward and backward extrapolations in RTM [23]. Since it is required to perform a RTM computation for each shot or transmitting antenna location, the computational cost of RTM is always a critical concern [35]. Therefore, RTM has not been widely used for GPR in practice due to the huge amount of data acquired during high-speed surveys [30]. On the other hand, the result of RTM is sensitive to the input of a velocity model [36]. Full waveform inversion [37] and travel-time tomography [31] can provide an estimate of the subsurface velocity structure as an initial model for RTM, but they incur additional computational cost and algorithm complexity. Since horizontally layered structures have been commonly encountered by GPR, such as concrete structures, asphalt pavements [7], sediments, and lunar regolith [10],

a horizontally layered velocity model is usually used for RTM of real GPR data [34], [38].

Besides the FDTD method, GPR simulation is also implemented in the frequency domain based on the Green's function of a point source over a layered structure [39]. To enhance the computation efficiency, a plane wave model with a spreading factor is proposed to approximate the layered medium Green's function [40]. A hybrid algorithm integrating FDTD method and Green's function is also proposed for GPR simulation in heterogeneous -2.5-D- media [41]. Due to the high efficiency of the frequency-domain simulation method, inversion of GPR data is usually conducted in the frequency domain to obtain the dielectric properties of the layered structure [40] and buried objects [42]. The Born approximation is commonly adopted to avoid the nonlinear effect of the integral equation and to setup the cost function for the scattering field at the receivers [23], [43].

In this paper, we propose an efficient frequency-domain RTM (FRTM) algorithm based on the layered medium dyadic Green's function (DGF), which is evaluated precisely by Sommerfeld integration. This FRTM is completely implemented in the frequency domain and in all three dimensions without the assumption of weak scattering and thus no Born approximation is made. In addition, in order to save computation time and resources, we take the advantage of the translation-invariance [44] of the layered medium DGFs to avoid the repetitive computation of DGFs for all the transmitters and receivers. A direct motivation of this paper is that a multi-input and multi-output (MIMO) GPR system is going to be launched to the moon by China's Chang-E 5 lunar exploration mission in 2019. This MIMO GPR system works in a stationary mode and will record only 132 GPR traces. In our previous work, a 2-D time domain RTM (TRTM) algorithm based on the FDTD method has been applied to the measured 132 GPR traces in laboratory, and the results validate the feasibility of the Chang-E 5 lunar exploration mission [34]. However, 3-D imaging of the subsurface rocks is desired for accurate geological interpretation and providing critical information for the regolith-drilling task on the moon, which restricts that the GPR data processing must be finished within three hours. In order to greatly enhance the computational efficiency and promote the practical applications of 3-D RTM to lunar exploration, as well as other engineering GPR survey, we apply the FRTM algorithm utilizing the DGF in layered media. Both the forward and backward extrapolation wavefields in the imaging region are computed by the multiplication between the frequency spectra of the excitation sources and the layered medium DGFs, which are evaluated independently for each sampling frequency. The final image is reconstructed by multiplication of the source and receiver wavefields in the frequency domain, instead of transforming them back to the time domain and adding them together for all shots. To evaluate the performance and efficiency of the proposed FRTM algorithm for both 2-D and 3-D imaging, we conducted two numerical and two laboratory experiments, and compared the consumption of computation time and memory between the FRTM algorithm based on the DGFs and the conventional TRTM algorithm based on the FDTD method.

This paper is organized as follows. In Section II, the algorithm of the FRTM is given in detail. The image condition, the computation of wavefield, and the execution of RTM in the frequency domain is discussed. In Section III, a numerical experiment is at first performed and the image results and computation cost are compared between FRTM and TRTM. Then, the second numerical experiment is implemented to study the effects of the polarization combination on the imaging results. In Section IV, the comparisons of the performance of FRTM and TRTM are also carried out for two laboratory experiments. Finally, in Sections V and VI, conclusions are drawn and some comments are given.

II. Methods

A. Imaging Condition in Frequency Domain

The algorithm of RTM consists of three main steps, i.e., forward propagation of the source wavefield, backward propagation of the receiver wavefield, and imaging condition. The zero-lag cross correlation of the source and receiver wavefields [45] is commonly used as the imaging condition as follows:

$$I(\mathbf{r}) = \int_0^T u_s(\mathbf{r}, t) u_r(\mathbf{r}, T - t) dt \tag{1}$$

where $\mathbf{r}$ is the location of the grid in the imaging domain and denotes (x, z) and (x, y, z) in the 2-D and 3-D cases, respectively, $I(\mathbf{r})$ is the reconstructed image generated from a common-source GPR gather, $u_s(\mathbf{r}, t)$ is the source wavefield propagated from the source, $u_r(\mathbf{r}, t)$ is the receiver wavefield, which is generated by extrapolating the time-reversed GPR waveform recorded by the receivers corresponding to the source, and T is the time window of the recorded GPR traces. Multiple sources or multiple source locations usually exist in the GPR data to be processed by RTM, and thus, the final reconstructed image is produced by stacking each RTM image for all the sources.

Due to the causality of the GPR signal, (1) can be rewritten in a convolution form as [46]

$$I(\mathbf{r}) = \int_0^T u_s(\mathbf{r}, t) u_r(\mathbf{r}, \tau - t) dt|_{\tau = T}. \tag{2}$$

Since the convolution in the time domain is corresponding to the multiplication of spectra in the frequency domain, (2) can be rewritten as

$$\begin{aligned} I(\mathbf{r}) &= \frac{1}{2\pi} \int_{-\infty}^{\infty} U_s(\mathbf{r}, \omega) U_r(\mathbf{r}, \omega) e^{j\omega\tau} d\omega|_{\tau = T} \\ &= \frac{1}{2\pi} \int_{-\infty}^{\infty} U_s(\mathbf{r}, \omega) U_r(\mathbf{r}, \omega) e^{j\omega T} d\omega \end{aligned} \tag{3}$$

where $U_s(\mathbf{r}, \omega)$ and $U_r(\mathbf{r}, \omega)$ are the Fourier transformation of the source wavefield $u_s(\mathbf{r}, t)$ and the receiver wavefield $u_r(\mathbf{r}, t)$, respectively.

B. Wavefield Computation for FRTM

The spectra of the wavefields, i.e., $\mathbf{U}_s(\mathbf{r}, \omega)$ and $\mathbf{U}_r(\mathbf{r}, \omega)$, in the imaging domain are directly computed by the multiplication of the DGFs and the spectra of the source wavelet and recorded GPR traces at the corresponding receivers, and their expressions

are given by [47]

$$\mathbf{U}_s(\mathbf{r},\omega) = \overline{\overline{\mathbf{G}}}(\mathbf{r},\mathbf{r}_s,\omega)\cdot\mathbf{S}(\mathbf{r}_s,\omega) \tag{4}$$

$$\mathbf{U}_r(\mathbf{r},\omega) = \overline{\overline{\mathbf{G}}}(\mathbf{r},\mathbf{r}_r,\omega)\cdot\mathbf{R}^*(\mathbf{r}_r,\omega)e^{-j\omega T} \tag{5}$$

where $\overline{\overline{\mathbf{G}}}$ is the DFG, $\mathbf{S}(\mathbf{r}_s,\omega)$ is the spectra of the source waveform excited at the source location $\mathbf{r}_s$, and $\mathbf{R}(\mathbf{r}_r,\omega)$ is the spectra of the recorded GPR trace at the receiver location $\mathbf{r}_r$. The complex conjugate denoted by the superscript * together with the multiplication factor $e^{-j\omega T}$ are corresponding to the time reversal of the recorded GPR trace.

The DFG is a second-order tensor for each frequency at each grid in the imaging domain, which means that our FRTM algorithm can be applied to GPR data recorded in any polarization combination. It links the vector field response to an electric source excitation with an arbitrary polarization [47], and can be written as

$$\overline{\overline{\mathbf{G}}}(\mathbf{r},\mathbf{r}_s,\omega) = \begin{bmatrix} g_{xx}(\mathbf{r},\mathbf{r}_s,\omega) & g_{xy}(\mathbf{r},\mathbf{r}_s,\omega) & g_{xz}(\mathbf{r},\mathbf{r}_s,\omega) \\ g_{yx}(\mathbf{r},\mathbf{r}_s,\omega) & g_{yy}(\mathbf{r},\mathbf{r}_s,\omega) & g_{yz}(\mathbf{r},\mathbf{r}_s,\omega) \\ g_{zx}(\mathbf{r},\mathbf{r}_s,\omega) & g_{zy}(\mathbf{r},\mathbf{r}_s,\omega) & g_{zz}(\mathbf{r},\mathbf{r}_s,\omega) \end{bmatrix} \tag{6}$$

and $\overline{\overline{\mathbf{G}}}(\mathbf{r},\mathbf{r}_r,\omega)$ has a similar form.

When a GPR measurement works in a perpendicular broadside mode and uses linearly polarized antennas for transmission and reception [48], only one polarization component of the electric field is recorded by GPR. Thus, only one component of the dyadic $\overline{\overline{\mathbf{G}}}$, e.g., $g_{yy}(\mathbf{r},\mathbf{r}_s,\omega)$ or $g_{yy}(\mathbf{r},\mathbf{r}_r,\omega)$, needs to be evaluated for computing spectra of the wavefields. In this way, the depolarization effects are neglected. In some situations when the multiple polarizations are considered, other components of $\overline{\overline{\mathbf{G}}}$ besides g_{yy} need to be computed. However, they have the similar translation-invariance properties as g_{yy} and the numerical evaluation is almost the same [49]. Therefore, in the following, we just take g_{yy} as an example and discuss the fast computation of the DGFs.

At a first glance, g_{yy} must be computed for all the field points $\mathbf{r}$ in the image domain corresponding to all the transmitters $\mathbf{r}_s$ and receivers $\mathbf{r}_r$ one by one. This is highly time consuming, especially for the 3-D RTM, because the layered medium DGF has no analytic solution and it can only be evaluated by the numerical Sommerfeld integration. The basic idea is to decompose the electromagnetic wave excited by radar antennas to a series of plane waves with different propagation directions through the 2-D spatial Fourier transform in the horizontal planes. The reflection and transmission coefficients for all the wave propagation directions are computed for multiple layers, and thus, the final wavefields at the observation points are the superposition of all these plane waves undergoing multiple reflection and transmission. The superposition is mathematically performed by the Sommerfeld integration. Detailed derivation and numerical evaluation of each component of the layered medium DGF can be found in [49]. Fortunately, the computation cost can be drastically reduced by virtue of the property of symmetry and horizontal translation-invariance of the DGF. These two properties can be easily proved from the expressions given in [49]. Briefly speaking, if we assume $\hat{z}$ is normal to the layer boundary, the g_{yy} of $\overline{\overline{\mathbf{G}}}(\mathbf{r},\mathbf{r}_s,\omega)$ can be expressed as

$$g_{yy}(\mathbf{r},\mathbf{r}_s,\omega) = g_{yy}(|x-x_s|,|y-y_s|,z,z_s,\omega) \tag{7}$$

and it has a similar expression for the $\overline{\overline{\mathbf{G}}}(\mathbf{r},\mathbf{r}_r,\omega)$. Only the g_{yy} for the arguments between $|x-x_s|_{\min}$ and $|x-x_s|_{\max}$ as well as $|y-y_s|_{\min}$ and $|y-y_s|_{\max}$ need to be computed. Others can be directly obtained by the property of symmetry and horizontal translation-invariance.

The computation of DGFs can be further accelerated by the Chebyshev interpolation in a horizontal plane. As shown in [49], (7) can be rewritten as

$$g_{yy}(\mathbf{r},\mathbf{r}_s,\omega) = g_{yy}(\rho,z,z_s,\omega) = g'_{yy}(\rho,z,z_s,\omega)f(\phi) \tag{8}$$

where $\rho = \sqrt{(x-x_s)^2+(y-y_s)^2}$, $\cos\phi = \frac{x-x_s}{\rho}$, $\sin\phi = \frac{y-y_s}{\rho}$, and $f(\phi)$ is a function of the azimuth angle ϕ. Obviously, the evaluation of g_{yy} can be performed through the Sommerfeld integration for different ρ values followed by the multiplication of trigonometric function values. Therefore, we first evaluate g'_{yy} for a limited number of sampled discrete ρ values between $\rho_{\min}$ and $\rho_{\max}$. The g_{yy} for any imaging point can be obtained by the Chebyshev interpolation in ρ followed by the multiplication of $f(\phi)$. The sampling rates of ρ are different for different frequencies. Numerical experiments show that the relative error of g_{yy} caused by the Chebyshev interpolation is less than 0.1% if the sampling point per wavelength (PPW) is larger than 4. So we set the PPW = 4 for the spatial sampling rate of ρ when g'_{yy} is computed. It should be noted that DGFs are evaluated independently for each frequency, and therefore are easily executed in a parallel computation mode. The Sommerfeld integration of g'_{yy} for all the z and z_s/z_r values and all the sampling frequencies is performed in advance and the results are saved in disk before the execution of FRTM.

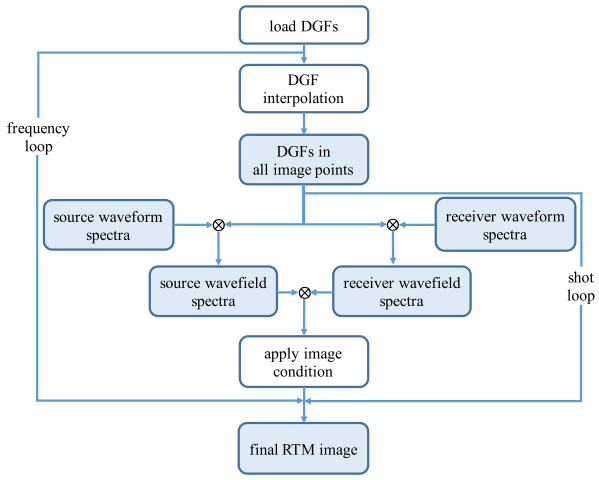

Fig. 1. Flowchart of the FRTM algorithm.

C. FRTM Algorithm

The flowchart of the FRTM algorithm is shown in Fig. 1. When FRTM is executed, the computed DFGs are loaded

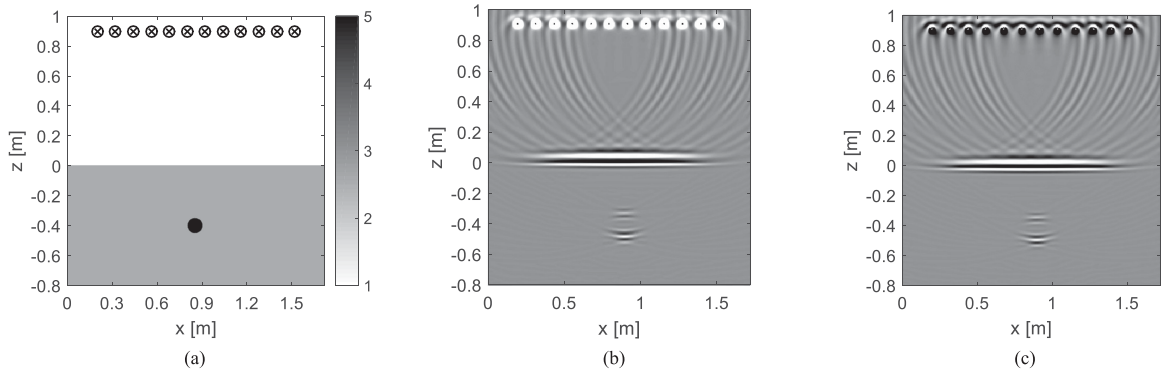

Fig. 2. (a) Numerical model. Comparison between the 2-D imaging results obtained. (b) By the conventional TRTM. (c) By the proposed FRTM using a synthetic MIMO GPR dataset from (a). A cylinder rock object with a radius of 5 cm is buried in the subsurface regolith.

into the memory at first. For each sampling frequency, the Chebyshev interpolation is performed to acquire the DGFs in all the field points in the imaging domain. The source wavefield spectra and the receiver wavefield spectra at all the image grids are computed by the multiplication of the DGFs and the source waveform spectra as well as the conjugates of the receiver waveform spectra according to (4) and (5). The final RTM image is reconstructed by the summation of the multiplication of wavefield spectra of the source and receivers for all the sampling frequencies according to (3). We do not save the DGFs for all the field points in disk since loading these values into memory is much more time consuming than the Chebyshev interpolation to acquire them from Sommerfeld integration results, and this is even more obvious in the 3-D FRTM. If multiple transmitting antennas or measurement locations exist in the GPR survey, we have to sum the GPR data acquired by the multiple transmitters, as illustrated by the "shot loop" in Fig. 1. In addition, the final RTM image is acquired by the summation over a series of discrete sampled frequencies in the effective frequency range of the GPR data, as illustrated by the "frequency loop" in Fig. 1. The frequency step is determined by the Nyquist criterion.

III. Numerical Experiments

At first, a 2-D numerical experiment using a MIMO GPR system is conducted to validate the proposed FRTM algorithm and to compare it with the TRTM based on FDTD, as shown in Fig. 2(a). The relative dielectric permittivity of the regolith and the larva rock are set to be 2.5 and 5, respectively, and the electric conductivity are 10^{-5} S/m and 10^{-4} S/m, respectively. It should be emphasized that the moisture effect on the regolith dielectric parameters is not considered in this paper since we are just mimic the Chang-E 5 lunar soil detection. To simulate the antenna array employed in Chang-E 5 Lunar exploration radar system, 12 antennas (infinitesimal electrical dipole sources polarized in the y direction) with a uniform spacing of 12 cm are used as a transmitting antenna in turn and the other 11 antennas are used as receiving antennas, and thus, 132 synthetic GPR traces are obtained by 12 FDTD simulations. A Blackman–Harris window (BHW) wavelet with a center frequency of 2 GHz is used for the source excitation. Direct coupling is muted from the simulated GPR traces. In order to compare two algorithms fairly, we run all the cases presented in this paper in the same computing server with 24 CPU cores (48 threads), 2.7-GHz speed, and 512 GB memory. The DGFs are computed in a parallel mode and the results are saved in the disk before performing the FRTM. Both TRTM and FRTM are executed sequentially using one thread of a single CPU core. In the 2-D FDTD computation of TRTM, the PPW is set to be 17, and the mesh size and the time step are 2.8 mm and 5 ps, respectively. The 2-D image region in this case has the size of 1.6×1.8 m ^{2}. For FRTM, the spatial sampling step for the field points in the image region is 4 mm in both the x and z directions. The source and receiver spectra are sampled from 20 MHz to 4 GHz with a frequency step of 20 MHz.

Fig. 2(b) and (c) show the 2-D images reconstructed by TRTM and FRTM using a half-space initial model, respectively. No difference can be discerned between the two reconstructed images except the phase difference at the source locations, which can be explained by the fact that the electric fields in the region very close to the source point cannot be accurately simulated by the FDTD method. Both the buried rock and the ground surface are clearly imaged, and the top and bottom interfaces of the rock can be identified. The computation resources consumed by the two RTM algorithms are given in Table I. The time for loading the DFGs into the memory before FRTM is negligible and not listed. For the FRTM, although the DFG interpolation and the RTM imaging are run in the same memory space, their running time can be distinguished. The FRTM algorithm consumes less than one fiftieth of the memory and 1% of the computation time cost by the TRTM algorithm. Since the DFGs can be computed in advance, a 2-D subsurface image can be produced from the real GPR data to be acquired by the Chang-E 5 lunar exploration mission by the FRTM algorithm in half a minute.

Then, we carried out a similar 2-D numerical experiment for the through-wall imaging application. The configuration is illustrated in Fig. 3(a). We also employ a MIMO GPR system. Ten infinitesimal electrical dipole antennas with a uniform spacing of 15 cm are placed 4 cm over the concrete wall and used as transmitters and receivers in turn. Thus, 99 synthetic GPR traces are obtained by ten FDTD simulations. A BHW wavelet with a center frequency of 2 GHz is used for the source ex-

TABLE I
COMPARISONS OF THE COMPUTATION CONSUMPTION BETWEEN TRTM AND FRTM FOR THE 2-D MIMO GPR NUMERICAL EXPERIMENT

		CPU cores/threads	Memory (MB)	Time (s)
FRTM	DGF computation	24/48	40	3380
	DGF interpolation	1/1	20	8
	RTM imaging			17
TRTM	RTM imaging	1/1	1400	10800

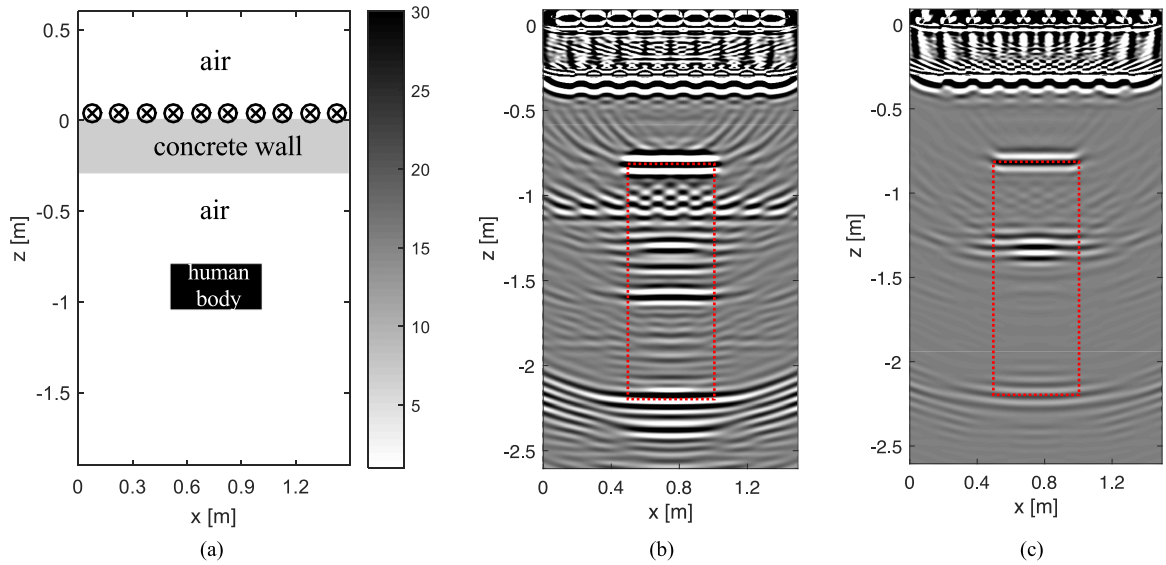

Fig. 3. (a) Through-wall numerical model. Comparison between the 2-D imaging results obtained by the proposed FRTM. (b) Using the copolarization. (c) Using cross polarization GPR data acquired over (a). A human body with a size of 50 cm × 25 cm is positioned 50 cm behind the 30-cm thick wall. Images in panel (b) and (c) are displayed in the same scale. The position of the human body in the migrated image is marked by a dotted red box.

citation. The concrete wall has a thickness of 30 cm, and the relative dielectric permittivity and conductivity are set to be 6.5 and 5×10^{-4} S/m, respectively. A human body with a size of 50 cm × 25 cm is positioned 50 cm behind the wall. The relative dielectric permittivity of the human body is 30 while the conductivity is 10^{-3} S/m.

Different from last case, we compare the imaging results by the FRTM algorithm using GPR data in different polarization combinations. A three-layer model (air-wall-air) is used as the initial model for the FTRM, and DFGs for g_{xx} and g_{xz} are calculated and saved in the hard disk. The imaging results from the co- [E_{xx} in Fig. 3(b)] and cross [E_{xz} in Fig. 3(c)] polarization GPR data are shown in Fig. 3(b) and (c), respectively. Obviously, the human body hidden behind the wall can be clearly imaged by both polarization combinations. The thickness of the human body is increased to 1.35 m in the migrated images, as indicated by the dotted red box. The reason is that the time delay of the electromagnetic waves passing through the human body is about 5.5 times of that in the air with the same thickness, due to the large electric contrast. In comparison, reflection from the human body is stronger in the copolarization channel than that in the cross polarization channel. Nevertheless, multiple reflections are more obvious in the co-polarization channel. For example, the ripple reflection at a depth of about 1.1 m is generated by the double bouncing signal inside the wall. While, it is hardly seen in the cross-polarization channel. The reason is that the cross polarization can mitigate the wall reflection, as well as its ringing, and thus highlight the reflection from the hidden human body [50].

IV. LABORATORY EXPERIMENTS

The results of a 2-D and a 3-D laboratory experiments are presented in this section. As shown in Fig. 4(a), a common-offset (CO) GPR profile containing 533 traces with a step of 4 mm was recorded over a sandpit by a commercial GPR system with the center frequency of 1.6 GHz. The IDS antennas are used and the distance between the transmitting and receiving antenna is about 4 cm. The source wavelet for RTM was recorded by the reflection from a flat metal plate buried at a depth of about 15 cm in the sand. A half-space initial model is used for both the TRTM and FRTM algorithms. The relative dielectric permittivity and electric conductivity of the sand are set to be 3.0 and 0.1 mS/m, respectively. For TRTM, the PPW of 2-D FDTD computation is set to be 13, and the mesh size and the time step are 3.4 mm and 6 ps, respectively. For FRTM, the spatial sampling step for the field points in the image region is 2 mm in both the x and z directions, and there are totally 1200 × 430 image pixels in

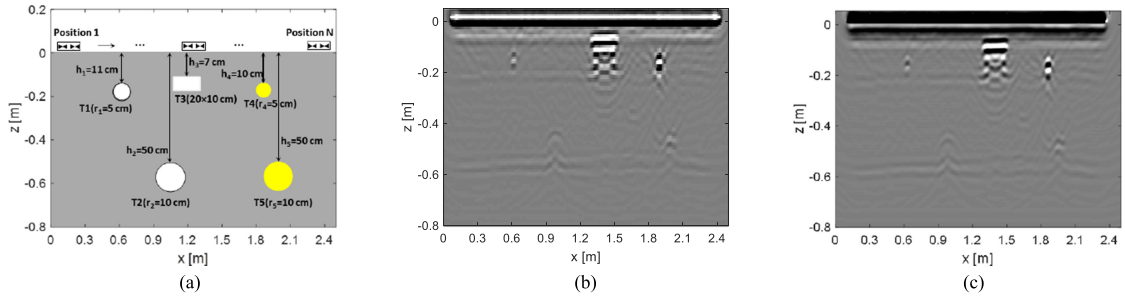

Fig. 4. (a) Experimental model. Comparison between the 2-D imaging results obtained. (b) By the conventional TRTM. (c) By the proposed FRTM using a measured CO GPR profile from (a). The two air-filled plastic pipes (marked by T1 and T2) and one air-filled glass cube (marked by T3) are marked by white color, and two metal pipes (marked by T4 and T5) are marked by yellow color.

TABLE II
COMPARISONS OF THE COMPUTATION CONSUMPTION BETWEEN TRTM AND FRTM FOR THE COMMON-OFFSET GPR LABORATORY EXPERIMENT

		CPU cores/threads	Memory (MB)	Time (s)
FRTM	DGF computation	24/48	50	34800
	DGF interpolation	1/1	40	61
	RTM imaging			373
TRTM	RTM imaging	1/1	2500	679000

the imaging region. The source and receiver spectra are sampled from 30 MHz to 6 GHz with a frequency step of 30 MHz. As shown in Fig. 4(b) and (c), the 2-D subsurface images reconstructed by the TRTM and FRTM are almost the same. The main difference is that the surface responses are almost out of phase. The reason is that the sources are placed on the ground surface and the electric fields near the source computed by the FDTD method are unreliable. All the buried pipes and the cube, as well as the bottom of the sandpit at a depth of about 58 cm, are clearly imaged. The comparison of computational costs by the two algorithms are given in Table II. Since the TRTM algorithm has to run two FDTD simulations for each source location, it consumes a computation time of about eight days, which is unaffordable for real GPR applications. While the FRTM algorithm needs calculating the DFGs only once, it consumes about 10 h, 1 min, and 6 min for the DFG computation, DFG interpolation, and the RTM imaging, respectively. The remarkable reduction in the memory and computation time by a magnitude of two orders is a great advantage of the proposed FRTM algorithm. For real GPR applications in engineering, such as urban utility detection, pavement and concrete structure inspections, and ice monitoring, the DFGs can be calculated in advance and saved in disk. In this way, the imaging time of FRTM is comparable as that of the conventional migration algorithms, such as diffraction stacking, F-K migration, etc. The high resolution and imaging accuracy benefited from RTM can facilitate the accurate interpretation of real GPR data in these engineering applications.

The 3-D laboratory experiment was conducted over a 7 m $\times$ 3 m $\times$ 2.5 m pit, which is filled with volcanic ash to mimic the lunar environment, as shown in Fig. 5(a). A 60 cm $\times$ 60 cm $\times$ 3 cm marble slab was buried at the depth of 1 m. The lunar regolith exploration GPR system employs 12 Vivaldi antennas and is equipped on the stationary lander. Each Vivaldi antenna has the size of 15 cm$\times$ 10 cm. The detailed layout of the Vivaldi antenna array can be found in [51]. The lander was placed over the ash pit and the height of the antenna from the ground surface is about 95 cm. Direct coupling was muted from the recorded 132 GPR traces according to the estimated arrival time of the surface reflection. A half-space model is used for both the TRTM and FRTM algorithms, and the relative dielectric permittivity and electric conductivity of the volcanic ash are set to be 3.0 and 10^{-5} S/m, respectively. The source wavelets radiated from the 12 Vivaldi antennas were recorded using a Vivaldi receiving antenna by lifting the lander at height of about 5 m from the ground surface. The recorded wavelet has a bandwidth of 4 GHz. Since we are only interested in the imaging of the subsurface domain, the DGFs in the above-ground domain are not calculated for the FRTM method. In contrast, the TRTM method has to take into account of the above-ground part, because the FDTD method has to extrapolate the wavefields from the source point. In TRTM, the PPW of 3-D FDTD computation is set to be 10 in this case, and the mesh size and the time step are 4.1 mm and 7.5 ps, respectively. In FRTM, the spatial sampling step in the subsurface domain is 4 mm in all the three directions, and there are totally 440 $\times$ 220 $\times$ 340 grids. The source and receiver spectra are sampled from 20 MHz to 4 GHz with a frequency step of 20 MHz.

The 3-D subsurface imaging results obtained by the two RTM algorithms are shown in Fig. 5(b) and (c). Almost no difference can be discerned from the reconstructed 3-D images by the two algorithms. Please note that the imaging resolution in the y direction is poorer than that in the x direction due to the limited aperture generated by the only two Vivaldi antennas deployed in the y direction. The comparison of the computational costs

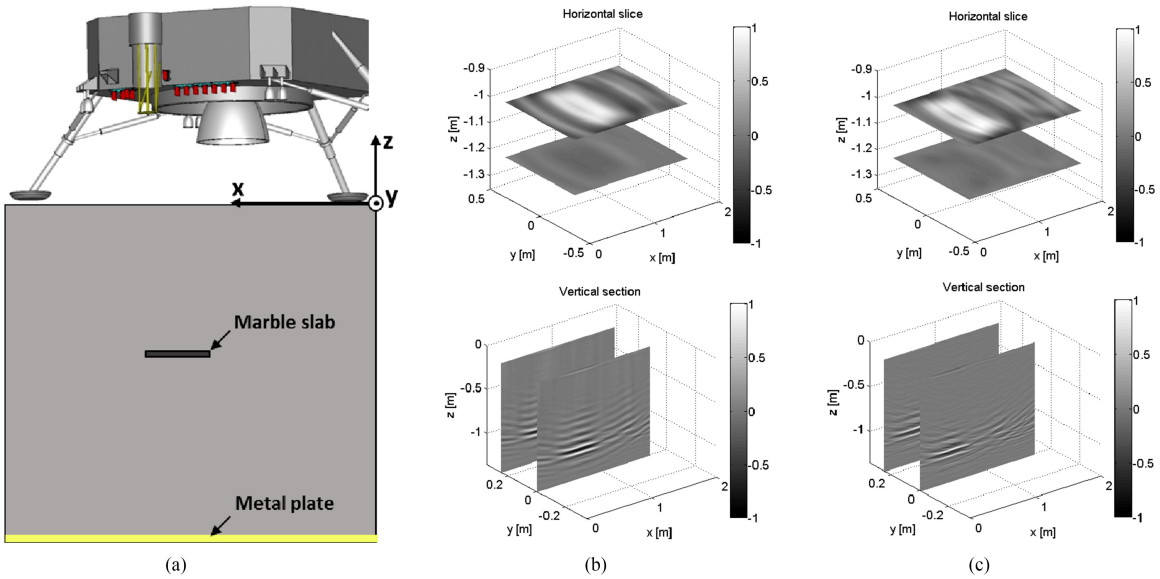

(a) (b) (c)

Fig. 5. (a) A schematic drawing of the laboratory experiment. Comparison between the 3-D imaging results obtained. (b) By the conventional TRTM. (c) By the proposed FRTM from a measured MIMO GPR dataset.

TABLE III
COMPARISONS OF THE COMPUTATION CONSUMPTION BETWEEN TRTM AND FRTM FOR THE GPR SYSTEM LABORATORY EXPERIMENT

		CPU cores/threads	Memory (MB)	Time (s)
FRTM	DGF computation	24/48	300	12500
	DGF interpolation	1/1	1200	7100
	RTM imaging			3570
TRTM	RTM imaging	1/1	5400	227000

by TRTM and FRTM is given in Table III. Since the 3-D FDTD simulation is computation-expensive, the TRTM consumed a memory of 5.4 GB and a computation time of almost three days. Since the DFGs can be computed and saved in disk in advance, the computation time needed for 3-D imaging by the FRTM algorithm is about 2.96 h, which can meet the requirement of the Chang-E 5 mission.

V. CONCLUSION

A FRTM algorithm based on the layered medium DFG has been presented in this paper. Through the results of the two numerical and the two laboratory experiments, it is concluded that the FRTM can reconstruct the same subsurface image as the conventional TRTM based on the FDTD method. The DFGs of the layered media need to be calculated only once due to its property of translation-invariance and symmetry in the horizontal plane. Moreover, since DFGs can be computed and saved in disk in advance, the imaging time required by the FRTM algorithm can be drastically reduced to less than a magnitude of two orders, compared with that of the TRTM. The laboratory experiment conducted using the lunar exploration GPR system validates that the GPR can produce a 3-D image of the possible rocks in the lunar regolith beneath the lander within three hours, which can provide important information for the critical drilling task of the Chang-E 5 mission of China.

VI. FUTURE REMARKS

The high efficiency of the proposed FRTM algorithm can promote the wide applications of RTM to field GPR data acquired for urban utility detection, pavement and concrete structure inspection, through-wall imaging, etc. With the development of the parallel computing algorithm in graphics processing unit, the FRTM could be able to yield real-time imaging of subsurface, and the high resolution and imaging accuracy benefited from RTM can facilitate the accurate interpretation of real GPR data in these engineering applications.

While processing air-launched GPR recorded on a platform of a car or an airplane, the advantage of the FRTM compared with the TRTM is even more obvious. The reason is that we only need to compute the DFGs in the interested subsurface domain and reconstruct the subsurface image. In contrast, the above-ground air space has to be included in the FDTD simulation for TRTM and this will drastically increase the computational costs. A stepped-frequency GPR system records data in the frequency domain and higher data quality can be achieved from the system stability, compared with the impulse GPR system [52]. When the FRTM algorithm is applied to a stepped-frequency GPR system, there is no need to transform the GPR data into the time domain and thus the subsurface image is directly produced. The third advantage of the FTRM is that the material dispersion caused by the soil moisture can be easily considered in the

implementation, since variant dielectric properties can be set at different frequencies and the corresponding DGFs can be simultaneously evaluated precisely.

In this paper, the actual GPR antenna has been simplified as a point source at its apparent phase center, and the antenna radiation pattern has not been considered in the FRTM algorithm. It has been demonstrated that accounting for the antenna radiation pattern in the migration or tomography algorithm can improve the subsurface GPR image [53], [54]. In view of the FTRM algorithm proposed in this paper, one of the feasible methods to include the antenna radiation pattern effect but without a high computation cost is to replace the GPR antenna, e.g., Vivaldi antenna, with a limited number of electromagnetic equivalent currents that can generate almost the same radiation pattern as the real antenna [55]. True reflection amplitude that represents the dielectric contrast and is independent of the antenna is expected to be obtained. However, this will be left as a future research work.

REFERENCES

[1] P. Paillou, G. Grandjean, N. Baghdadi, E. Heggy, T. August-Bernex, and J. Achache, "Subsurface imaging in south-central Egypt using low-frequency radar: Bir Safsaf revisited," *IEEE Trans. Geosci. Remote Sens.*, vol. 41, no. 7, pp. 1672–1684, Jul. 2003.

[2] H. Miyamoto, J. Haruyama, T. Kobayashi, and S. Rokugawa, "Mapping the structure and depth of lava tubes using ground penetrating radar," *Geophys. Res. Lett.*, vol. 32, no. 21, pp. 1–5, 2005.

[3] B. Guan, A. Ihamouten, X. Dérobert, D. Guilbert, S. Lambot, and G. Villain, "Near-field full-waveform inversion of ground-penetrating radar data to monitor the water front in limestone," *IEEE J. Sel. Topics Appl. Earth Observ.in Remote Ses.*, vol. 10, no. 10, pp. 4328–4336, Oct. 2017.

[4] A. Saintenoy and J. W. Hopmans, "Ground penetrating radar: Water table detection sensitivity to soil water retention properties," *IEEE J. Sel. Topics Appl. Earth Observ.in Remote Ses.*, vol. 4, no. 4, pp. 748–753, Dec. 2011.

[5] H. Jang, S. Kuroda, and H. J. Kim, "Efficient electromagnetic imaging of an artificial infiltration process in the vadose zone using cross-borehole radar," *IEEE Geosci. Remote Sens. Lett.*, vol. 8, no. 2, pp. 243–247, Mar. 2011.

[6] H. Liu, X. Xie, J. Cui, K. Takahashi, and M. Sato, "Groundwater level monitoring for hydraulic characterization of an unconfined aquifer by common mid-point measurements using GPR," *J. Environ. Eng. Geophys.*, vol. 19, no. 4, pp. 259–268, Dec. 2014.

[7] H. Liu and M. Sato, "In situ measurement of pavement thickness and dielectric permittivity by GPR using an antenna array," *NDT E Int.*, vol. 64, no. 2, pp. 65–71, 2014.

[8] F. Benedetto, F. Tosti, and A. M. Alani, "An entropy-based analysis of GPR data for the assessment of railway ballast conditions," *IEEE Trans. Geosci. Remote Sens.*, vol. 55, no. 7, pp. 3900–3908, Jul. 2017.

[9] V. Ciarletti, C. Corbel, D. Plettemeier, P. Cais, S. M. Clifford, and S.-E. Hamran, "WISDOM GPR designed for shallow and high-resolution sounding of the Martian subsurface," *Proc. IEEE*, vol. 99, no. 5, pp. 228–232, May 2011.

[10] L. Xiao *et al.*, "A young multilayered terrane of the northern Mare Imbrium revealed by Chang' E-3 mission," Science, vol. 347, no. 6227, pp. 1226–1229, Mar. 2015.

[11] G. Valerio, A. Galli, P. M. Barone, S. E. Lauro, E. Mattei, and E. Pettinelli, "GPR detectability of rocks in a Martian-like shallow subsoil: A numerical approach," *Planet. Space Sci.*, vol. 62, pp. 31–40, 2012.

[12] X. Feng, M. Sato, and C. Liu, "Hand-held GPR imaging using migration for irregular data," *IEEE J. Sel. Topics Appl. Earth Observ.in Remote Ses.*, vol. 4, no. 4, pp. 799–803, Dec. 2011.

[13] I. Giannakis, A. Giannopoulos, and C. Warren, "A realistic FDTD numerical modeling framework of ground penetrating radar for landmine detection," *IEEE J. Sel. Topics Appl. Earth Observ.in Remote Ses.*, vol. 9, no. 1, pp. 37–51, Jan. 2016.

[14] J. Schofield, D. Daniels, and P. Hammerton, "A multiple migration and stacking algorithm designed for land mine detection," *IEEE Trans. Geosci. Remote Sens.*, vol. 52, no. 11, pp. 6983–6988, Nov. 2014.

[15] M. Sato, Y. Hamada, X. Feng, F. N. Kong, Z. Zeng, and G. Fang, "GPR using an array antenna for landmine detection," *Near Surface Geophys.*, vol. 2, no. 4, pp. 7–13, 2004.

[16] J. Gazdag, "Wave equation migration with the phase-shift method," *Geophysics*, vol. 43, no. 43, pp. 1342–1351, 1978.

[17] J. Song, Q. H. Liu, P. Torrione, and L. Collins, "Two-dimensional and three-dimensional NUFFT migration method for landmine detection using ground-penetrating radar," *IEEE Trans. Geosci. Remote Sens.*, vol. 44, no. 6, pp. 1462–1469, Jun. 2006.

[18] J. I. Halman, K. A. Shubert, and G. T. Ruck, "SAR processing of ground-penetrating radar data for buried UXO detection: Results from a surface-based system," *IEEE Trans. Antennas Propag.*, vol. 46, no. 7, pp. 1023–1027, Jul. 1998.

[19] L. Zhou, C. Huang, and Y. Su, "A fast back-projection algorithm based on cross correlation for GPR imaging," *IEEE Geosci. Remote Sens. Lett.*, vol. 9, no. 12, pp. 228–232, Mar. 2012.

[20] S. Demirci, E. Yiğit, I. H. Eskidemir, and C. Özdemir, "Ground penetrating radar imaging of water leaks from buried pipes based on back-projection method," *NDT E Int.*, vol. 47, no. 2, pp. 35–42, 2012.

[21] C. Özdemir, S. Demirci, E. Yiğit, and B. Yilmaz, "A review on migration methods in B-scan ground penetrating radar imaging," *Math. Probl. Eng.*, vol. 2014, pp. 1–16, 2014.

[22] A. Benedetto and L. Pajewski, *Civil Engineering Applications of Ground Penetrating Radar*. Berlin, Germany: Springer, 2015.

[23] C. J. Leuschen and R. G. Plumb, "A matched-filter-based reverse-time migration algorithm for ground-penetrating radar data," *IEEE Trans. Geosci. Remote Sens.*, vol. 39, no. 5, pp. 929–936, May 2001.

[24] J. Zhu and L. R. Lines, "Comparing of Kirchhoff and reverse-time migration methods with application to prestack depth imaging of complex structures," *Geophysics*, vol. 63, no. 4, pp. 1166–1176, 1998.

[25] H.-W. Zhou, *Practical Seismic Data Analysis*. New York, NY, USA: Cambridge Univ. Press, 2014.

[26] E. Baysal, D. D. Kosloffs, and J. W. C. Sherwood, "Reverse time migration," *Geophysics*, vol. 48, no. 11, pp. 1514–1524, 1983.

[27] W.-F. Chang and G. A. McMechan, "Reverse-time migration of offset vertical seismic profiling data using the excitation-time imaging condition," *Geophysics*, vol. 51, no. 1, pp. 67–84, 1986.

[28] W. Chung, S. Pyun, H. S. Bae, C. Shin, and K. J. Marfurt, "Implementation of elastic reverse-time migration using wavefield separation in the frequency domain," *Geophys. J. Int.*, vol. 189, no. 3, pp. 1611–1622, 2012.

[29] Z. Wang, H. Ding, G. Lu, and X. Bi, "Reverse-time migration based optical imaging reverse," *IEEE Trans. Med. Imag.*, vol. 35, no. 1, pp. 273–281, Aug. 2016.

[30] E. Fisher, G. A. McMechan, A. P. Annan, and S. W. Cosway, "Examples of reverse-time migration of single-channel," *Geophysics*, vol. 57, no. 4, pp. 577–586, 1992.

[31] H. Zhou and M. Sato, "Subsurface cavity imaging by crosshole borehole radar measurements," *IEEE Trans. Geosci. Remote Sens.*, vol. 42, no. 2, pp. 335–341, Feb. 2004.

[32] J. H. Bradford, "Reverse-time prestack depth migration of GPR data from topography for amplitude reconstruction in complex environments," *J. Earth Sci.*, vol. 26, no. 6, pp. 791–798, 2015.

[33] H. Yang, T. Li, N. Li, Z. He, and Q. H. Liu, "Time-gating-based time reversal imaging for impulse borehole radar in layered media," *IEEE Trans. Geosci. Remote Sens.*, vol. 54, no. 5, pp. 2695–2705, Dec. 2016.

[34] H. Liu, Z. Long, B. Tian, F. Han, G. Fang, and Q. H. Liu, "Two-dimensional reverse-time migration applied to GPR With a 3-D-to-2-D data conversion," *IEEE J. Sel. Topics Appl. Earth Obsserv.in Remote Ses.*, vol. 10, no. 10, pp. 4313–4320, Oct. 2017.

[35] F. Deng and G. A. McMechan, "True-amplitude prestack depth migration," *Geophysics*, vol. 72, no. 3, pp. S155–S166, 2007.

[36] W. Dai, P. Fowler, and G. T. Schuster, "Multi-source least-squares reverse time migration," *Geophys. Prospecting*, vol. 60, no. 4, pp. 681–695, 2012.

[37] S. Liu, L. Lei, L. Fu, and J. Wu, "Application of pre-stack reverse time migration based on FWI velocity estimation to ground penetrating radar data," *J. Appl. Geophys.*, vol. 107, pp. 1–7, 2014.

[38] W.-F. Chang and G. A. McMechan, "Elastic reverse-time migration," *Geophysics*, vol. 52, no. 10, pp. 1365–1375, 1987.

[39] S. Lambot, E. C. Slob, I. van den Bosch, B. Stockbroeckx, and M. Vanclooster, "Modeling of ground-penetrating radar for accurate characterization of subsurface electric properties," *IEEE Trans. Geosci. Remote Sens.*, vol. 42, no. 11, pp. 2555–2568, Nov. 2004.

[40] S. Maiti, S. K. Patra, and A. Bhattacharya, "GPR modeling for rapid characterization of layered media," *Progress in Electromagn. Res. B*, vol. 63, pp. 217–223, 2015.

[41] K. J. Ellefsen, D. Croizé, A. T. Mazzella, and J. R. McKenna, "Frequency-domain Green's functions for radar waves in heterogeneous 2.5D media," *Geophysics*, vol. 74, no. 3, pp. J13–J22, 2009.
[42] F. Soldovieri *et al.*, "GPR estimation of the geometrical features of buried metallic targets in testing conditions," *Progress in Electromagn. Res. B*, vol. 49, pp. 339–362, 2013.
[43] P. Meincke, "Linear GPR inversion for lossy soil and a planar air-soil interface," *IEEE Trans. Geosci. Remote Sens.*, vol. 39, no. 12, pp. 2713–2721, Dec. 2001.
[44] X. Millard and Q. H. Liu, "A fast volume integral equation solver for electromagnetic scattering from large inhomogeneous objects in planarly layered media," *IEEE Trans. Antennas Propag.*, vol. 51, no. 9, pp. 2393–2401, Sep. 2003.
[45] N. D. Whitmore and L. R. Lines, "Vertical seismic profiling depth migration of a salt dome flank," *Geophysics*, vol. 51, no. 5, pp. 1365–1375, 1986.
[46] K. Xu, B. Zhou, and G. A. McMechan, "Implementation of prestack reverse time migration using frequency-domain extrapolation," *Geophysics*, vol. 75, no. 2, pp. S61–S72, 2010.
[47] H. Liu, Z. Deng, F. Han, Y. Xia, Q. H. Liu, and M. Sato, "Time-frequency analysis of air-coupled GPR data for identification of delamination between pavement layers," *Construction Building Mater.*, vol. 154, pp. 1207–1215, 2017.
[48] J. L. Porsani, E. Slob, R. S. Lima, and D. N. Leite, "Comparing detection and location performance of perpendicular and parallel broadside GPR antenna orientations," *J. Appl. Geophys.*, vol. 70, no. 1, pp. 1–8, 2010.
[49] K. A. Michalski and J. R. Mosig, "Multilayered media green's functions in integral equation formulations," *IEEE Trans. Antennas Propag.*, vol. 45, no. 3, pp. 508–519, Mar. 1997.
[50] W. Zhang, A. Hoorfar, C. Thajudeen, and F. Ahmad, "Full polarimetric beam-forming algorithm for through-the-wall radar imaging," *Radio Sci.*, vol. 46, p. RS0E16, 2011.
[51] W. Lu, Y. C. Ji, B. Zhou, and G. Y. Fang, "Design of an array antenna system for Chang' E-5 LRPR," in *Proc. 16th Int. Conf. Ground Penetrating Radar*, Hong Kong, 2016, pp. 1–4.
[52] H. Liu, B. Xing, J. Zhu, B. Zhou, F. Wang, X. Xie, and Q. H. Liu, "Quantitative stability analysis of ground penetrating radar systems," *IEEE Geosci. Remote Sens. Lett.*, vol. 15, no. 4, pp. 522–526, Apr. 2018.
[53] D. Comite, A. Galli, I. Catapano, and F. Soldovieri, "The role of the antenna radiation pattern in the performance of a microwave tomographic approach for GPR imaging," *IEEE Trans. Geosci. Remote Sens.*, vol. 10, no. 10, pp. 4337–4347, Oct. 2017.
[54] R. Streich and J. Kruk, "Accurate imaging of multicomponent GPR data based on exact radiation patterns," *IEEE Trans. Geosci. Remote Sens.*, vol. 45, no. 1, pp. 93–103, Jan. 2007.
[55] Y. Álvarez, F. Las-Heras, and M. R. Pino, "Reconstruction of equivalent currents distribution over arbitrary three-dimensional surfaces based on integral equation algorithms," *IEEE Trans. Antennas Propag.*, vol. 55, no. 12, pp. 3460–3468, Dec. 2007.

Hai Liu (S'11–M'13) received the B.E. and M.E. degrees in civil engineering from Tongji University, Shanghai, China, in 2007 and 2009, respectively, and the Ph.D. degree in environmental studies from Tohoku University, Sendai, Japan, in 2013.

From April 2013 to March 2014, he was with the Center for Northeast Asian Studies, Tohoku University, as a Research Fellow. From July 2014 to July 2017, he was an Assistant Professor with the Institute of Electromagnetics and Acoustics, Xiamen University, Xiamen, China. He is currently an Associate Professor with the School of Civil Engineering, Guangzhou University, Guangzhou, China. His current research interests include development of ground-penetrating radar systems and algorithms for a wide variety of applications, such as nondestructive testing in civil engineering, environmental monitoring, archeological investigation, and lunar exploration.

Dr. Liu received the Young Researcher Award of the 14th International Conference on Ground Penetrating Radar in 2012 and the Excellent Paper Award of the IET International Radar Conference in 2013.

Zhijun Long's photograph and biography not available at the time of publication.

Feng Han (M'17) received the B.S. degree in electronic science from Beijing Normal University, Beijing, China, in 2003, the M.S. degree in geophysics from Peking University, Beijing, China, in 2006, and the Ph.D. degree in electrical engineering from Duke University, Durham, NC, USA, in 2011.

He is currently an Assistant Professor with the Institute of Electromagnetics and Acoustics, Xiamen University, Xiamen, China. His research interests include ionosphere remote sensing by radio atmospherics, electromagnetic full-wave inversion by integral equations, subsurface imaging, and the design of an electromagnetic detection system.

Guangyou Fang received the B.S. degree in electrical engineering from Hunan University, Changsha, China, in 1984, and the M.S. and Ph.D. degrees in electrical engineering from Xian Jiaotong University, Xian, China, in 1990 and 1996, respectively. From 1990 to 1999, he was an Engineer, Associate Professor, and Professor with the China Research Institute of Radio wave Propagation. From 2000 to 2001, he was a Visiting Scholar with the University of Trieste and International Center for Science and High Technology, Italy. From 2001 to 2003, he was a special foreign Research Fellow of the Japan Society for Promotion of Science, working with the Professor M. Sato with Tohoku University, Japan. He was the PI of CE-3 lunar penetrating radar. Since 2004, he has been a Professor with the Institute of Electronics of Chinese Academy of Sciences (IECAS), Beijing, China, the Director of the Key Lab of Electromagnetic Radiation and Sensing Technology of CAS, and the Deputy Director of IECAS from 2013. He has published more than 300 papers in refereed journals and conference proceedings. His research interests include electromagnetic field theory, ultrawideband radar, ground-penetrating radar, lunar and mars exploration radar, geophysical electromagnetic exploration technology, and THz Imaging.

Qing Huo Liu (S'88–M'89–SM'94–F'05) received the B.S. and M.S. degrees in physics from Xiamen University, Xiamen, China, in 1983 and 1986, respectively, and the Ph.D. degree in electrical engineering from the University of Illinois at Urbana-Champaign, Champaign, IL, USA, in 1989.

From September 1986 to December 1988, he was with the Electromagnetics Laboratory, University of Illinois at Urbana-Champaign, as a Research Assistant, and from January 1989 to February 1990, as a Postdoctoral Research Associate. From 1990 to 1995, he was a Research Scientist and Program Leader with Schlumberger-Doll Research, Ridgefield, CT, USA. From 1996 to May 1999, he was an Associate Professor with New Mexico State University. Since June 1999, he has been with Duke University, Durham, NC, USA, where he is currently a Professor with the Department of Electrical and Computer Engineering. He has published more than 400 papers in refereed journals and 500 papers in conference proceedings. His research interests include computational electromagnetics and acoustics, inverse problems, and their applications in nanophotonics, geophysics, biomedical imaging, and electronic packaging.

Dr. Liu is a Fellow of the Acoustical Society of America, a Fellow of the Electromagnetics Academy, and a Fellow of the Optical Society of America. He currently serves as the Deputy Editor-in-Chief of the Progress in Electromagnetics Research, an Associate Editor for the IEEE TRANSACTIONS ON GEOSCIENCE AND REMOTE SENSING, and an Editor of the *Journal of Computational Acoustics*. He also served as the Guest Editor for the PROCEEDINGS OF THE IEEE. Since August 2015, he has been serving as the Founding Editor-in-Chief of the new the IEEE JOURNAL ON MULTISCALE AND MULTIPHYSICS COMPUTATIONAL TECHNIQUES. He serves as an IEEE Antennas and Propagation Society Distinguished Lecturer for 2014–2016. He received the 1996 Presidential Early Career Award for Scientists and Engineers from the White House, the 1996 Early Career Research Award from the Environmental Protection Agency, and the 1997 CAREER Award from the National Science Foundation. He received the 2017 ACES Technical Achievement Award.